Materials Today Chemistry 26 (2022) 101117

Contents lists available at ScienceDirect

Materials Today Chemistry

journal homepage: www.journals.elsevier.com/materials-today-chemistry/

Investigation of the electrocatalytic activity of bismuth-substituted pyrochlore $Y_2Sn_2O_7$ for the voltammetry determination of the antipsychotic drug

Raj Karthik [a], Karuppaiah Balamurugan [b], Shen-Ming Chen [b, *], Ramaraj Sukanya [c], Prajakta R. Chavan [a], Van Quang Nguyen [a, d], Jae-Jin Shim [a, **], Carmel B. Breslin [c]

[a] School of Chemical Engineering, Yeungnam University, Gyeongsan, Gyeongbuk 38541, Republic of Korea
[b] Department of Chemical Engineering and Biotechnology, National Taipei University of Technology, No. 1, Section 3, Zhongxiao East Road, Da'an District, Taipei City, Taiwan
[c] Department of Chemistry, Maynooth University, Maynooth, Co. Kildare, W23 FH6, Ireland
[d] Department of Road and Bridge Engineering, The University of Da Nang-University of Science and Technology, 54 Nguyen Luong Bang, Da Nang 550000, Viet Nam

ARTICLE INFO

Article history:
Received 23 April 2022
Received in revised form
25 July 2022
Accepted 29 July 2022
Available online 31 August 2022

Keywords:
Pyrochlore oxide
Cation (Bi^{3+}) substitution
Yttrium tin oxide
Chlorpromazine sensor
Real sample analysis

ABSTRACT

Pyrochlore oxides are considered active candidates for various electrochemical applications due to their cationic charges and anionic deficiency. At the same time, the cationic substitution of pyrochlore is a crucial parameter to improve the catalytic activity of electrode materials. Against this background, this article aims to synthesize bismuth-substituted defective pyrochlore-yttrium tin oxide nanoparticles ($Bi_{0.6}Y_{1.4}Sn_2O_7$; BYSO NPs) and construct an electrochemical sensor for the antipsychotic chlorpromazine (CHPMZ). The catalyst was prepared by co-precipitation technique followed by thermal treatment. The analytical methods, such as p-XRD, FT-IR, TGA, and XPS, confirmed the successful substitution of Y^{3+} by Bi^{3+}. The morphology of the as-prepared catalysts was analyzed by the FE-SEM and TEM techniques, which shows that the size of nanoparticles is ~20–30 nm. From the CV results, the cationic substitution enhances the electrocatalytic oxidation of CHPMZ due to the intrinsic activity enhancement by the substitution with a large size cation and the anionic deficiency of the pyrochlore structure. Moreover, the heterogeneous rate constant of CHPMZ on BYSO/SPCE was calculated to be 4.49×10^{-3} cm/s, indicating that the oxidation of CHPMZ on BYSO/SPCE is quasi-reversible. The electrode modified with BYSO NPs showed wider linear ranges (0.01–58.41 μM, 78.41–1158 μM), high sensitivity (1.03 μA/μM/cm^2) with a low detection limit of 3 nM. The modified electrodes showed good selectivity, repeatability, and excellent stability for the detection of CHPMZ. Moreover, the constructed sensor showed promising results in practical analysis with good recovery in human blood serum and urine samples.

1. Introduction

Chlorpromazine (2-chloro-10-(3-dimethylaminopropyl) phenothiazine; CHPMZ) is a well-known antipsychotic that belongs to the group of phenothiazine derivatives with an aliphatic side-chain structure. CHPMZ is widely used to treat bipolar disorder, depressive illness, schizophrenia, and manic-depressive disorder [1]. It acts by blocking postsynaptic dopaminergic D2 receptors in the brain's mesolimbic and prefrontal cortex regions, thereby reducing the positive symptoms of schizophrenia. CHPMZ has also been prescribed to reduce psychomotor disorders, agitation, hyperkinetic aggression, and anxiety [2]. In addition, CHPMZ works on various receptors in the central nervous system to produce antiemetic, anticholinergic, hypothermic, hypotensive, and anesthetic effects [3]. However, when CHPMZ is taken in large amounts, it can cause various health problems in humans, which have been described in detail in previous articles [4]. It is necessary to develop sensitive and innovative techniques to monitor CHPMZ concentration. Techniques such as flow injection [5], HPLC [6,7], potentiometry [8], electrochemiluminescence, and capillary zone electrophoresis [9,10] have been developed for the determination of CHPMZ. However, these techniques require sophisticated

* Corresponding author.
** Corresponding author.
E-mail addresses: smchen78@ms15.hinet.net (S-M. Chen), jjshim@yu.ac.kr (J-J. Shim).

https://doi.org/10.1016/j.mtchem.2022.101117
2468-5194/

instrumentation, are time-consuming, and require large reagents. In contrast, electrochemical techniques have the potential to provide high selectivity, rapid response, simplicity, and high sensitivity in the analysis of biological and pharmaceutical compounds [3,55]. However, electrode modifiers play an essential role in an electrochemical sensor, a transducer between the electrode surface and the electrolyte medium. They enhance electrocatalytic activity with improved sensitivity, selectivity, and reproducibility by reducing overvoltage and overcoming the slow kinetics of many electrode processes.

Recently, cubic pyrochlore metal oxides have attracted the attention of researchers due to their advantageous properties, such as conventional synthesis methods, compositional flexibility, and high thermal and electrical stability. The cubic pyrochlore structure (space group *Fd-3m*, $Z = 8$) with the general formula $A_2^{2+/3+}B_2^{5+/4+}O_6O'$ can be obtained from fluorite solid solutions. The cations form a face-centered cubic arrangement, and 1/8 of the anions are removed to ensure charge neutrality [11]. The flexibility in composition and anionic vacancies make pyrochlore oxides a successful material for applications such as nuclear waste encapsulation, transistors, electrocatalysts, and fast ionic conductors [12–14]. In particular, stannate-based pyrochlores have been synthesized for more than 40 years, so a comprehensive knowledge of their structural trends, thermodynamic properties, disorder, and non-stoichiometry has been developed [14]. Moreover, lanthanide-based stannate ($Ln_2Sn_2O_7$: Ln = Y, Ce, La, Pr, Sm, Nd, Gd) has been successfully used as electrocatalysts [15–20]. These oxides have remarkable chemical and physical properties such as tunable electronic structure, high melting point, and high chemical and thermal stability. They also contain a high density of oxygen vacancies, which gives them exciting properties for various electrocatalytic applications [21]. Based on the crystal structure of the pyrochlore, the formula can be described as $A_2B_2O_6O'$, where the two oxygen species consist of a network of BO_6 octahedral arranged across corners, with the A and O′ atoms occupying the interstitial sites. Consequently, the O anion connects two components to create a network linking the cations of the A- and B-sites. Thus, the O anion connects two components to form a network between the cations of the A- and B-sites. In contrast, the O′ anion of a different type forms only the 'A-O-A' bond with the cation of the A site. It is known that oxygen vacancies generally occur preferentially at the interstitial O′ sites rather than at the O sites. This type of oxygen vacancy can induce charge transfer through the emptiness and increases the electrocatalytic activity [19–21]. Among $Ln_2Sn_2O_7$, $Y_2Sn_2O_7$ (YSO) has attracted much attention and has been used in numerous applications, such as a heterogeneous catalyst for CO oxidation, piezoelectricity, and dielectric resistance to radiation damage. In addition, YSO serves as a host material for doping with various lanthanide and transition metal ions and has been used for photocatalytic applications [22,23]. However, studies on the electrocatalytic application of YSO are limited compared to other pyrochlore oxides. *Nithyadharseni* et al. synthesized YSO nanoparticles by molten salt method and used them as anode material in lithium-ion batteries [24]. *Sharma* et al. synthesized YSO nanoparticles by solid-state method and showed 89% capacity retention in lithium-ion batteries [25]. The catalytic activity of metal oxides was modulated by partial replacement of the existing metal cation with an aliovalent or isovalent metal ion. Introduction of a new metal cation that changed the electronic environment of the host matrix. The ionic radius and electronegativity of guest and host atoms affect the electrochemical activity of electrode materials. The substituent leads to changes in the oxidation state of the active metal (aliovalent substitution only), the concentration of oxygen vacancies, the coordination environment, or the electronic band structure (insulator to semiconductor transition, and semiconductor-conductor transition [26,27]. *Ansari* et al. synthesized cerium-doped lanthanum cobalt oxides and lanthanum manganese oxides as perovskite materials, which exhibit better catalytic activity for benzyl alcohol oxidation reactions. [28,29]. Moreover, the partial aliovalent substitution of Ru^{4+} by Y^{3+} showed higher OER activity than the unsubstituted material. The increased catalytic activity arises from oxygen defects in the lattice caused by the change in oxidation state from Ru^{4+} to Ru^{5+} during the substitution of Y^{3+} [30]. Interestingly, *Muller* et al. synthesized isovalently substituted ruthenium pyrochlore oxide to develop the OER activity. The substituted pyrochlore showed higher catalytic activity than the pure pyrochlore with the property of unchanged oxidation of the active band center (Ru) metal [31].

Bismuth is a post-transition metal with a higher electronegativity (x = 2.02) than the transition metals and rare earth elements. Recently, *Horn* et al. have successfully substituted Bi^{3+} ions into the strontium-cobalt perovskite material. The substituted perovskite material shows higher catalytic activity for the OER reaction than the pure perovskite. Due to the higher electronegativity and Lewis acidic nature of the Bi^{3+} ion, the hydroxide affinity of the perovskite increased and promoted the OER [32]. Inspired by the above literature, we have synthesized the partially substituted Y^{3+} ion with Bi^{3+} in pyrochlore-yttrium tin oxide nanoparticles ($Bi_{0.6}Y_{1.4}Sn_2O_7$; BYSO NPs). The electrode modified with BYSO NPs was successfully used to detect CHPMZ. Various analytical and spectroscopic techniques analyzed the as-prepared BYSO NPs. Voltammetry methods performed electrocatalytic applications. When a screen-printed carbon electrode (SPCE) was modified with the BYSO NPs, improved electrocatalytic activity was observed for the electrochemical detection of CHPMZ. The proposed BYSO/SPCE is low cost and shows good electrocatalytic activity and high selectivity for the determination of CHPMZ.

2. Experimental

2.1. Materials and methods

The required chemicals (all analytical grade), such as urea [$CO(NH_2)_2$], chlorpromazine [CHPMZ], yttrium nitrate hexahydrate [$Y(NO_3)_3.6H_2O$], sodium stannate trihydrate [$Na_2SnO_3.3H_2O$], bismuth oxide (Bi_2O_3), disodium hydrogen phosphate, and sodium dihydrogen phosphate, were obtained from Sigma-Aldrich, Taiwan. Electrochemical experiments were performed in a phosphate buffer solution (0.05 M) and it was prepared with appropriate amounts of monosodium and disodium hydrogen phosphate. The pH of the electrolyte was adjusted by adding proper amounts of aqueous HCl and NaOH.

2.2. Preparation of BYSO NPs

BYSO NPs were prepared by a combination of co-precipitation followed by calcination. First, 30 mL solutions of 0.1 M $Y(NO_3)_3.6H_2O$ and $Na_2SnO_3.3H_2O$ were prepared separately and then mixed with 50 mL DI water in a beaker. Under magnetic stirring, urea (3 g/10 mL DI water) was added dropwise and stirred for another hour at room temperature.

Then the precipitate was centrifuged and washed thoroughly with water and ethanol to give the pure hydroxide precursors of yttrium tin ($YSn(OH)_6$). To prepare bismuth substituted yttrium stannate (BYSO), 30% bismuth oxide (Bi_2O_3) was mixed with ($YSn(OH)_6$) and well ground with a mortar and pestle. The well ground Bi_2O_3/$YSn(OH)_6$ mixture and $YSn(OH)_6$ were individually calcined at 800 °C for 6 h. For control studies, yttrium oxide (Y_2O_3) and tin oxide (SnO_2) were prepared separately from nitrate precursors of yttrium and tin by the precipitation method. This method is shown in Scheme 1.

2.3. Analytical methods

The crystal phases of the as-synthesized catalysts (SnO_2, Y_2O_3, YSO NPs, BYSO NPs) were analyzed by powder X-ray diffraction (p-XRD, PANalytical X'pert- PRO MPD). The functional groups were analyzed by Fourier transform infrared spectroscopy (FT-IR, PerkinElmer Two series spectrophotometer). X-ray photoelectron spectroscopy (XPS, Thermo Scientific Instrument) determined the elements' binding energies and the exact energy level. The elements' morphology, texture, and composition were analyzed by field-emission scanning electron microscopy (FE-SEM, Hitachi S-4800) and transmission electron microscopy (TEM, Philips, CM-200). Electrochemical studies were performed using CHI instruments (CV—CHI 611A; DPV-CHI 900) with a conventional three-electrode system, namely BYSO NPs/SPCE (working electrode), Sat (KCl).Ag/AgCl (reference electrode), and platinum wire (counter electrode). A 0.05 M PB solution saturated with N_2 was used as the supporting electrolyte for the electrochemical studies.

2.4. Electrode modification and preparation of real sample

3 mg of the synthesized BYSO NPs were well dispersed in 1 mL of DI water under sonication for 10 min. Before the electrode preparation step, the working electrode (Screen-printed carbon electrode; SPCE) was carefully washed with DI water to wash out impurities and improve surface wettability. Then, 6 μL of the prepared dispersions were applied to the surface of the SPCE and dried in an air oven. The catalyst-loaded SPCE was used as a working electrode for the electrochemical experiments.

Human blood serum and urine samples were collected from a hospital in Taiwan for real sample analysis. Both samples were mixed with EDTA and methanol to remove the proteins and residues in the blood serum and urine samples. Then the real samples were centrifuged at 6000 rpm/10 min, and the supernatant was collected. The collected supernatant was mixed with 0.05 M PBS (pH 7.0) to form a stock solution. A known concentration of CHPMZ was added to the stock solutions to mimic the CHPMZ in the real samples.

3. Results and discussion

3.1. X-ray diffraction and FTIR analysis

Fig. 1A, B shows the XRD patterns of the prepared YSO, BYSO NPs, Y_2O_3, and SnO_2. From Fig. 1A(a), it can be seen that the ($Y_2Sn_2O_7$, YSO NPs) diffraction peaks at angles 29.8°, 34.5°, 49.6°, 59°, 61.9°, and 72.8° correspond to hkl planes (222), (400), (440), (622), (444), and (800) of the cubic phase of the pure YSO NPs. The results also show that the as-prepared YSO NPs are in the form of a single phase. The corresponding values of the lattice parameters, a = b = c= (10.3) nm and α = β = γ = 90° of the YSO NPs, agree well with the standard card [JCPDS. 88—0508]. The XRD pattern for the BYSO NPs shown in Fig. 1A(b) is similar with diffraction peaks at angles of 29.6°, 34.4°, 49.4°, 58.7°, 61.6°, and 72.5°, which again agree with the following plane values: (222), (400), (440), (622), (444), and (800). These planes agree well with the standard card [JCPDS.

88-0503]. A slight shift in the XRD peak positions was observed, indicating the successful substitution of yttrium by bismuth in the crystal lattice of the YSO NPs. Moreover, the substitution of yttrium by bismuth affects the crystal lattice and increases the lattice parameters, a = b = c = 10.4, and the cell volume also increases to 1129.6×10^6 pm^3. The lattice parameters were increased due to the large ionic size and lone pair of electrons of the Bi^{3+} ion. Furthermore, no additional impurities such as SnO_2 or Y_2O_3 were observed in the YSO or BYSO NPs. The corresponding XRD patterns of SnO_2 and Y_2O_3 are shown in Fig. 1B (a, b), and it is evident that these oxide phases are not present in either the YSO or BYSO NPs. This XRD study indicates the formation of a pure phase of pyrochlore oxide BYSO NPs. The XRD lattices are consistent with the cubic crystal structure of pyrochlore with eight formula units per unit cell. The Y(III) ions are surrounded by eight oxygen atoms in a distorted cubic polyhedron, while the Sn(IV) ions are coordinated by six oxygen atoms in an octahedral configuration. The Bi^{3+} ions replace the Y^{3+} ions in the lattice sites of YSO, as shown by the XRD (*i.e.*, the slight peak shift and increased lattice parameters observed in the YSO NPs). We conclude that a simple co-precipitation followed by a calcination process can achieve the substitution of Y^{3+} by Bi^{3+} in YSO NPs with Bi at a relatively low temperature. In addition, the average crystal size of the BYSO NPs was estimated using the Debye-Scherer equation (see equation (1)). Here, D is the grain size of the particle, λ is the wavelength (CuK, 0.15), β is the full-width half-maximum, and the k value is 0.9. From Equation (1), the crystalline particle size of the pyrochlore BYSO NPs was 14.4 nm.

$$D = k\lambda/\beta\cos\theta \quad (1)$$

In addition, the functional groups of the as-prepared BYSO and YSO NPs were analyzed by FTIR spectroscopy. Fig. S1A shows the FTIR spectra of BYSO and YSO NPs as they were synthesized. The pure YSO sample shows two vibrational bands at 449 and 647 cm^{-1}. The high and low intensity bands at 647 cm^{-1} and 930 cm^{-1} correspond to the Sn—O stretching and O—Sn—O bending vibrations, respectively. The band observed at 449 cm^{-1} is attributed to the stretching vibration of the Y—O bond in the pyrochlore

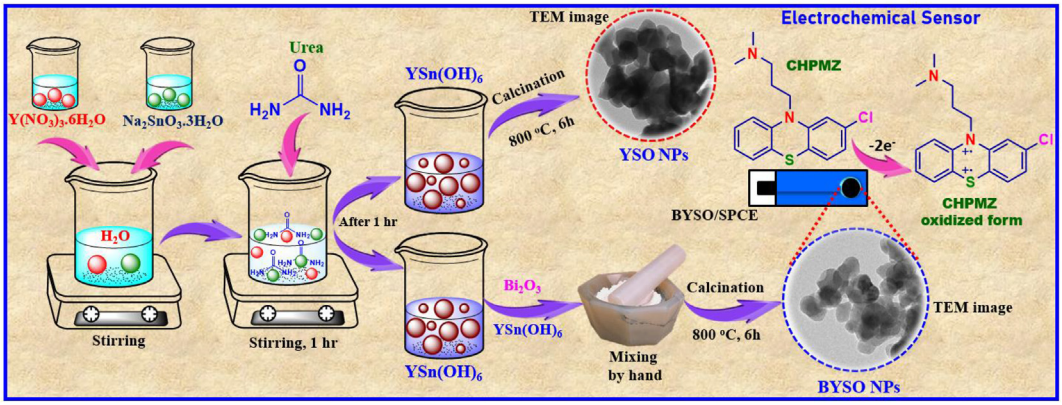

Scheme 1. Schematic representation of the experimental system: synthesis, fabrication, and electrochemical sensor application of YSO NPs and BYSO NPs.

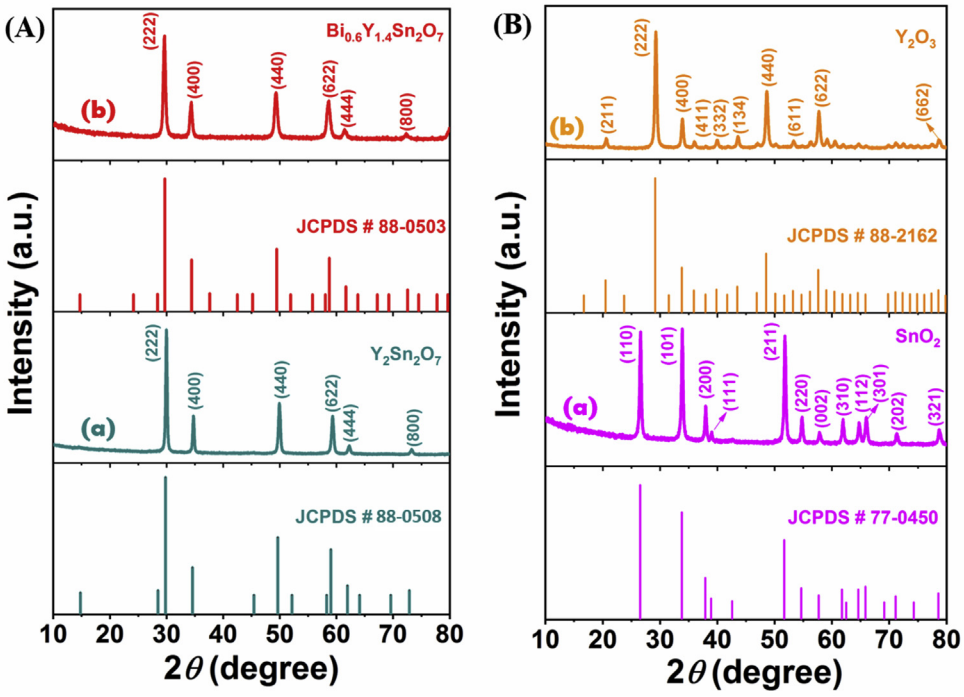

Fig. 1. (A) XRD of BYSO NPs, and YSO NPs. (B) XRD of SnO_2 (c) and Y_2O_3 (d).

structure [33,34]. After the substitution of Bi in the YSO NPs, the FTIR spectrum shows an additional peak at 510 cm^{-1}, which represents the Bi—O vibrational mode [35]. The stretching vibrations of Sn—O and Y—O were slightly shifted to lower wavenumbers, confirming the successful incorporation of the Bi^{3+} ion into the YSO pyrochlore structure. The reason for the blue shift is as follows: during the substitution of Y^{3+} by Bi^{3+}, the O—Sn—O bond was increased due to the large ionic radii of Bi^{3+}. The remaining bands between 1300 and 1500 cm^{-1} represent the H—O—H vibrations in the KBr sample [34]. The peak shifts detected in the XRD and FTIR analyses of the BYSO NPs confirm the successful substitution of the Bi^{3+} ion in the crystal lattice of the YSO NPs.

3.2. X-ray photoelectron spectroscopy

XPS was used to investigate the presence of elements and their valence in the BYSO and YSO NPs. Fig. 2 shows the overview spectrum and core level spectrum of YSO and BYSO NPs. The overview spectrum of YSO (Fig. 2A) indicates the presence of yttrium (Y), tin (Sn), and oxygen (O). The overview spectrum of BYSO (Fig. 2A) shows the peaks corresponding to bismuth (Bi) and the similar elements (Y, Sn, O) present in the YSO spectrum. The XPS spectra of the core level of Y 3d in YSO (Fig. 2B) show two peaks corresponding to Y $3d_{5/2}$ (157.0 eV) and Y $3d_{3/2}$ (159.1 eV), indicating the presence of Y^{3+}. The XPS spectrum of Y 3d in BYSO (Fig. 2B) shows a triplet, Y $3d_{5/2}$, located at 157.0 eV, and Y $3d_{3/2}$ was mixed with Bi $4f_{7/2}$ (158.7 eV). In addition.

The intensity of Y $3d_{3/2}$ is higher than that of Y $3d_{5/2}$ in BYSO due to mixing with Bi 4f (158.7 eV). The two peaks at 158.7 and 164.0 eV correspond to Bi $4f_{7/2}$ and Bi $4f_{5/2}$, respectively, showing the successful substitution of Y^{3+} by Bi^{3+} in YSO [36,37]. YSO and BYSO (Fig. 2C) show the Sn 3d doublet spectrum with similar binding energies at 485.6 eV (Sn $3d_{5/2}$) and 494.1 eV (Sn $3d_{3/2}$), indicating the presence of Sn^{4+}. The magnified O 1s of YSO and BYSO show a doublet corresponding to the M − O (529.4 eV) and O—H (530.4 eV; YSO, and 530.9; BYSO) bonds. The lattice oxygen bond intensity is higher in BYSO than in YSO, which can be attributed to the presence of Bi^{3+} ions [37] and an increase in the lattice oxygen. These XPS results also confirm the successful substitution of Bi^{3+} in the YSO NPs.

3.3. Morphological characterization

FE-SEM and HR-TEM analysis investigated the surface and textural properties of the as-prepared YSO and BYSO NPs. Fig. 3(A—F) shows images at different resolutions of both YSO (A-C) and BYSO (D-F) NPs. These images show that the YSO and BYSO NPs are composed of many NPs that coalesce into larger particles (see Fig. 3A). Comparing the microscopic pictures of YSO and BYSO, there is no significant change in morphology due to the substitution of Bi^{3+}. The structural nature of the YSO and BYSO NPs was analyzed in more detail using HR-TEM analysis. Fig. 4A exhibits the HR-TEM image of YSO NPs, revealing that ununiformed nanoparticles were formed with the size of ~20—30 nm. The HR-TEM images of BYSO NPs were shown in Fig. 4B—E with different magnifications. From these images, it can be seen that BYSO NPs (Fig. 4B) have a size of about ~20—30 nm. Fig. 4D shows the presence of distinct lattice fringes of BYSO NPs. Moreover, the crystalline nature of the fabricated BYSO NPs is indicated by the bright selected area electron diffraction (SAED) pattern in Fig. 4F. Finally, the accompanying EDS analysis of the BYSO NPs, shown in Fig. 3G confirms the presence of Bi, Y, Sn, and O without other impurities. Again, these surface analysis results are direct evidence that the bismuth substituted in pyrochlore YSO NPs are in the form of pure NPs with no structural changes. Finally, the morphological analysis revealed that no significant topology changes were observed after the substitution of Bi^{3+} into the crystal lattice of YSO NPs.

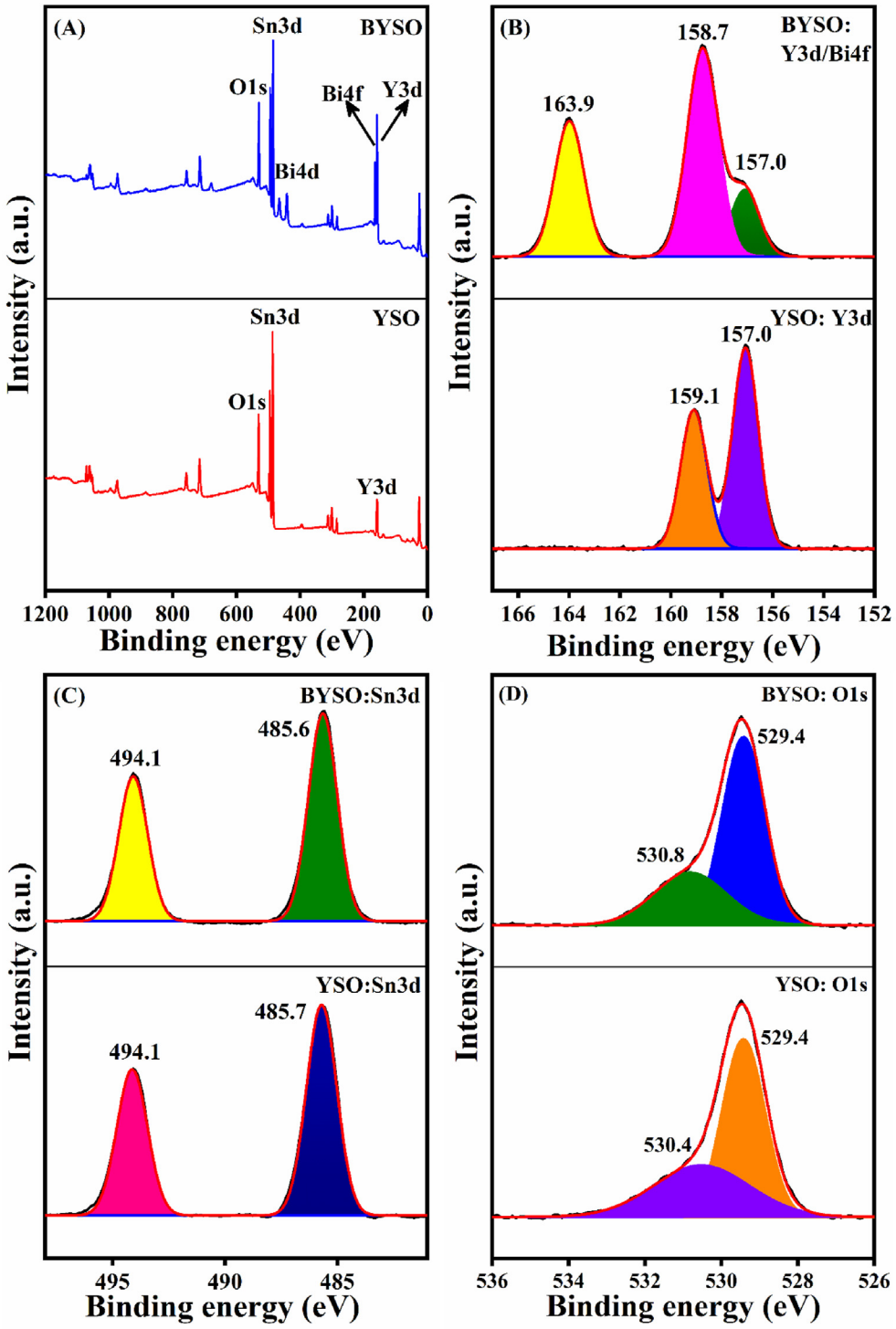

Fig. 2. (A) Survey spectrum of BYSO and YSO. High-resolution XPS spectrum of Y 3d (B), Sn 3d (C), and O 1s (D).

3.4. Thermogravimetric (TGA) analysis

Thermal analysis of the prepared materials was investigated by TGA analysis. The TGA curve of the pure YSO NPs (Fig. S1B) shows a weight loss of 1% in the first step, from 400 °C to 800 °C, indicating that the weight loss is due to the evaporation loss of water or other matrix presents during the synthesis process. This is also evidence of the high thermal stability of the pure YSO phase. The TGA curve of BYSO NPs also shows a weight loss of 4.5%, which mainly occurs in two steps; the first weight loss of 1.4% occurs up to 400 °C and the second of 3.1% from 400 °C to 900 °C, which is due to the evaporation of the adsorbed water molecule on the particle surface and the decomposition of the substituted bismuth ions or the other matrix (SnO or YnO) [38–40]. Moreover, the thermal stability of BYSO NPs is slightly lower than that of pure YSO NPs, which might be related to the introduction of Bi into the pure YSO NPs.

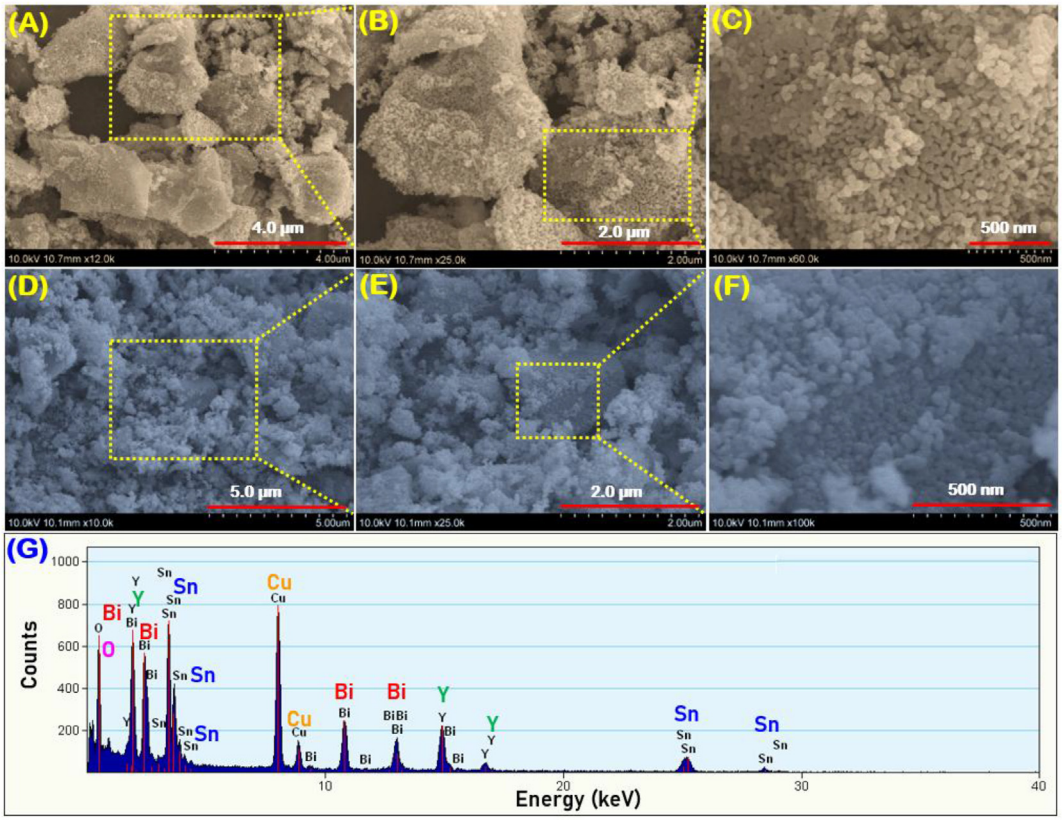

Fig. 3. FE-SEM images of YSO NPs (A–C) and BYSO NPs (D–F). (G) EDS analysis of BYSO NPs.

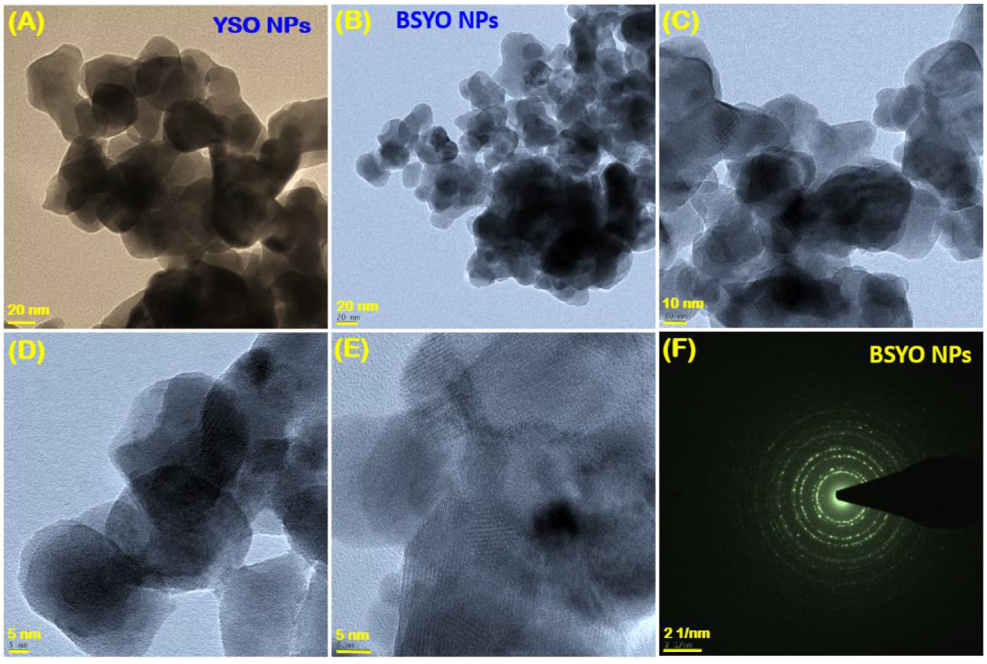

Fig. 4. TEM images of (A) YSO NPs, and (B–E) BYSO NPs. (F) SAED pattern of as-prepared BYSO NPs.

3.5. Electrochemical characterization of different electrodes

EIS spectroscopy was used to obtain information on the electron transfer resistance of the electroactive materials. Fig. 5A shows the Nyquist plots recorded with different electrodes, including the unmodified SPCE, SnO_2/SPCE, Y_2O_3/SPCE, YSO/SPCE, and BYSO/SPCE containing 5 mM $[Fe(CN)_6]^{3-/4-}$ dissolved in 0.1 M KCl. From Fig. 5A, it can be seen that the general shapes of the plots

are similar, with a semicircle combined with a diffusion process at higher frequencies. However, there is a noticeable variation in the diameter of the semicircles, with the bare SPCE having the lowest R_{ct} value, implying the highest electrical conductivity. On the other hand, the SPCE was modified with SnO_2, the charge transfer resistance (1001 Ω) would increase significantly due to the semiconducting properties of SnO_2. A slightly lower R_{ct} value (771 Ω) is observed with Y_2O_3 as the electrode modifier because it has a lower charge transfer resistance than SnO_2. When the SPCE is modified with YSO, the R_{ct} value (683 Ω) decreases even further due to the synergistic effects between the two different metal cations and the ionic conductivity resulting from the defective structure of the pyrochlore oxides. Interestingly, the bismuth substituted YSO (BYSO) shows much (292 Ω) lower R_{ct} values than the other modified electrodes and is very similar to the unmodified SPCE.

Fig. 5B shows the CV curves recorded with the different modified electrodes at 50 mV/s in 5 mM $[Fe(CN_6)]^{3-/4-}$ dissolved in a 0.1 M KCl supporting electrolyte. It can be observed that the bare SPCE exhibits the highest anodic and cathodic peak currents, I_{pa} and I_{pc}, and a smaller distance between the peak separation than the other modified electrodes. Conversely, the modified electrodes show lower I_{pa} and I_{pc} and higher peak-to-peak separations. These results are consistent with the electrostatic repulsion between the anionic metal complex $[Fe(CN_6)]^{3-/4-}$ and the metal oxides [34], resulting in sluggish kinetics. The BYSO-modified SPCE exhibits the highest I_{pa} and I_{pc} values and the lowest peak-to-peak separation among electrocatalyst-modified electrodes. The data from CV agree well with the EIS results, indicating that the BYSO NPs have good conductivity.

The $[Fe(CN_6)]^{3-/4-}$ probe was also used to investigate the effects of scan rate on peak currents and to estimate the electrochemical surface area of the modified SPCE electrodes. Fig. 5C shows the CVs recorded at different scan rates from 20 to 120 mV/s at the BYSO/SPCE. It can be seen that both I_{pa} and I_{pc} increase with scan rate. When the I_{pa} and I_{pc} values are plotted as a function of the square root of the scan rate, a linear curve is obtained, indicating that a diffusion-controlled reaction occurs at the BYSO-modified SPCE. The linear plot is shown in Fig. 5D along with the linear regression equations (I_{pa} (μA) = −7.972 ($\nu^{1/2}$) −3.521 (R^2 = 0.997) and I_{pc} (μA) = 7.086 ($\nu^{1/2}$) −6.989 (R^2 = 0.996)). Using the Randles-Sevcik relationship given in Equation (2), the electrochemically active surface area of BYSO/SPCE was calculated using the linear regression equation for the forward peak oxidation currents (I_{pa} vs. $\nu^{1/2}$).

$$I_{pa}\ (\mu A) = (2.69 \text{ X } 10^5)\ n^{3/2}\ ACD^{1/2}\ \nu^{1/2} \quad (2)$$

In Equation (2), n (n = 1) corresponds to the number of electrons transferred, *A* represents the surface area, C (5×10^{-3} mol/L) corresponds to the concentration of $[Fe(CN)_6]^{3-/4-}$, and D is the diffusion coefficient (D = 7.60×10^{-6} cm^2/s). From Equation (2), the electrochemically active surface area of BYSO/SPCE is 0.08 cm^2. In addition, the scan rate study was also performed on the other modified electrodes. The corresponding CV curves and their respective linear plots are shown in Fig. S2 A, C, E (CVs of SnO_2/SPCE, Y_2O_3/SPCE, and YSO/SPCE) and Fig. S2 B, D, F (linear plots of I_{pa}, I_{pc} vs. $\nu^{1/2}$). From the linear regression equations, the electrochemically active surface area of the modified electrodes was determined to be 0.055 cm^2 (SnO_2/SPCE), 0.058 cm^2 (Y_2O_3/SPCE),

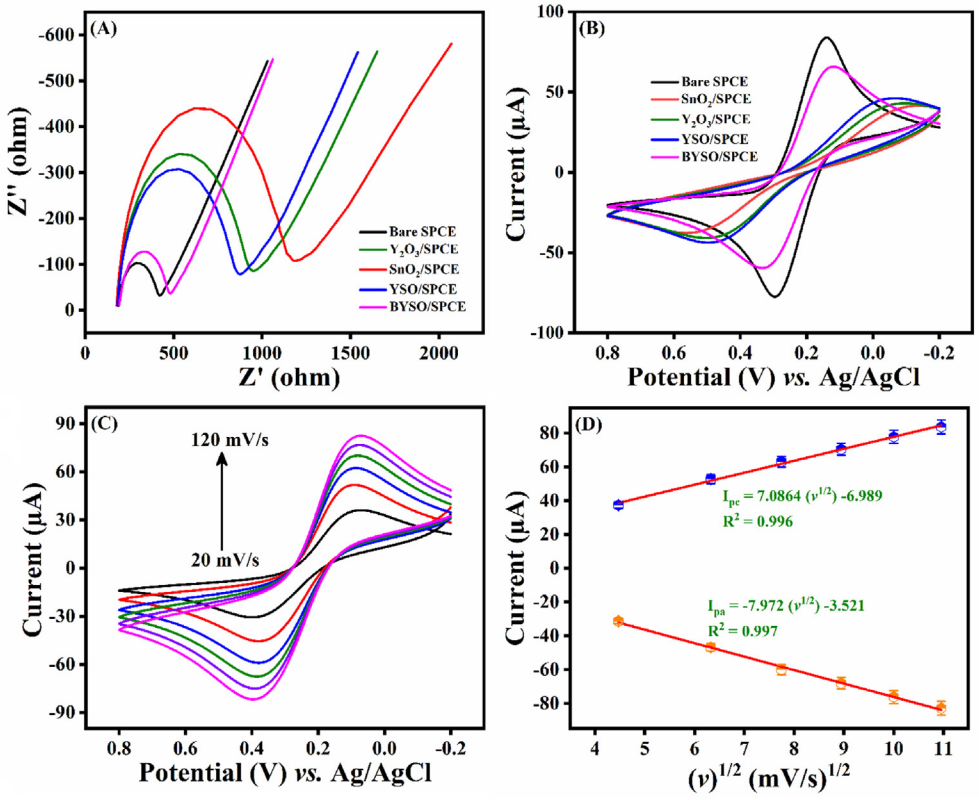

Fig. 5. (A) Nyquist diagram of bare SPCE, SnO_2/SPCE, Y_2O_3/SPCE, YSO/SPCE, and BYSO/SPCE. (B) CVs of 5 mM $[Fe(CN)_6]^{3-/4-}$ on unmodified and modified electrodes in 0.1 M KCl at a potential scan rate of 50 mV/s (C) CV curves of BYSO/SPCE at different scan rates (20–120 mV/s) in 5 mM $[Fe(CN)_6]^{3-/4-}$ 0.1 M KCl. (D) Calibration plot between I_{pa}, I_{pc} and the square root of the scan rate for BYSO/SPCE.

and 0.062 cm^2 (YSO/SPCE). This analysis shows that the BYSO/SPCE has the highest electrochemical active surface area and good electrical conductivity.

3.6. Electrochemical sensor behavior of the different electrodes versus CHPMZ

To investigate the electrochemical sensing capability of the different modified and unmodified electrodes, CV was performed between the potential limits of +0.2 V to +1.0 V in 0.05 M PBS (pH 7.0) with 150 μM CHPMZ. Fig. 6A shows the CV curves of the bare SPCE and the SPCE modified with SnO_2, Y_2O_3, YSO, and BYSO, recorded at a potential scan rate of 50 mV/s. The bare SPCE and all modified electrodes show a distinct anodic peak at +0.69 V to +0.72 V. The bare SPCE leads to the lowest anodic peak (I_{pa} = 4.91 μA) at a peak potential of 0.72 V, which is due to the slow electron transfer kinetics to the CHPMZ. After modification of the SPCE with SnO_2, the anodic peak current increases with a slight negative potential shift (I_{pa} = 6.31, E_{pa} = +0.718 V). A further increase in the oxidation current of CHPMZ was observed with Y_2O_3 (I_{pa} = 6.50 μA, E_{pa} = +0.696 V). This increased catalytic activity of SnO_2/SPCE and Y_2O_3/SPCE is due to the ionic conductivity of the metal oxides. A further enhancement of the anodic current (I_{pa} = 6.9 μA) was observed for YSO/SPCE. This enhancement was attributed to the pyrochlore oxides having two different metal cations and an anionic vacancy. This type of defect can enhance the adsorption of molecules and increase the catalytic activity by ionic conductivity. Accordingly, the enhanced detection of CHPMZ on YSO/SPCE was attributed to the anionic vacancy of the pyrochlore structure and the synergistic effect of the two different metal cations [41–43]. Finally, the SPCE modified with BYSO shows the highest anodic peak current (I_{pa} = 7.8 μA), which is significantly higher than the peak currents of the other modified electrodes. Since the ionic radius of Bi^{3+} (117 p.m.) is larger than the ionic radius of Y^{3+} (104 p.m.), the defective sites in the pyrochlore structure are enhanced. These defective sites increase charge transfer efficiency and facilitate the adsorption of CHPMZ molecules. Moreover, Bi^{3+} has higher electronegativity and acidic Lewis character than Y^{3+} [32], which can also improve the anodic oxidation of CHPMZ. The performances of the SPCE electrodes and the modified SPCE are summarized in Fig. 6B, which shows a comparative bar graph of the anodic peak currents. This analysis indicates that the SPCE modified with BYSO has 1.60, 1.26, 1.23, and 1.17 times higher current than the bare SPCE, SnO_2/SPCE, Y_2O_3/SPCE, and YSO/SPCE, respectively.

Fig. 6C shows the voltammograms recorded at 50 mV/s for different concentrations of CHPMZ at the BYSO/SPCE. Higher peak currents are observed with increasing CHPMZ concentration, as shown in Fig. 6D. A linear relationship is obtained when the peak current is plotted as a function of CHPMZ concentration. The corresponding linear regression equation is I_{pa} (μA) = 0.046C (μM) + 0.777 (R^2 = 0.990). In addition, a good linear relationship (R^2 = 0.998) was obtained between the logarithmic of the peak current (log I_{pa}) and the logarithmic of the CHPMZ concentration (log C) (Fig. S3A). Considering the kinetics of the oxidation of CHPMZ and replacing the reaction rate *R* by the current, the reaction order can be estimated from the slope of the plot in Fig. S3A, as shown in Equation (3). In this case, the slope is 0.85, which is fairly close to a first-order reaction. This result indicates that the electrochemical oxidation of CHPMZ at the BYSO/SPCE

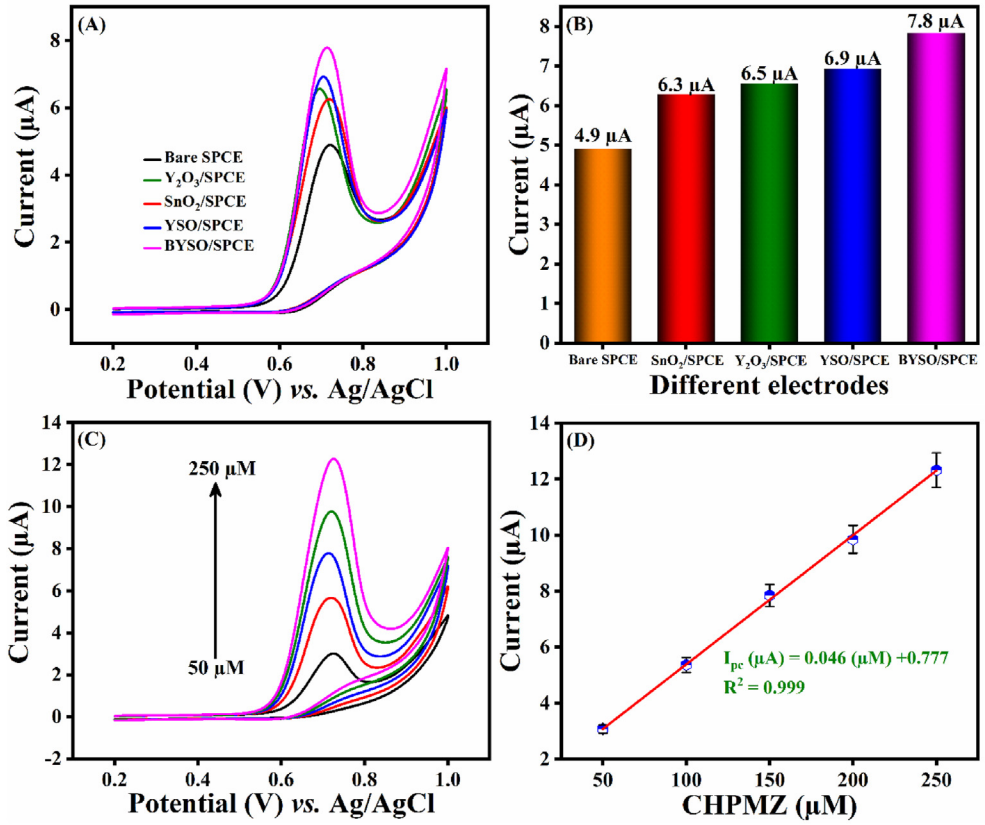

Fig. 6. (A) CVs of 150 μM CHPMZ on different electrodes, namely, SnO_2/SPCE, Y_2O_3/SPCE, YSO/SPCE, and BYSO/SPCE. (B) Comparison of anodic current of 150 μM CHPMZ at different electrodes. (C) CVs of BYSO/SPCE with the gradual addition of CHPMZ from 50 to 250 μM. (D) Calibration plot: I_{pa} (μA) *vs.* concentration of CHPMZ. The selected parameters for all the experiments: Scan rate: 50 mV/s; Potential: +0.2 V to +1.0 V; Supporting electrolyte: N_2 saturated 0.05 M PBS (pH 7.0).

electrode is approximately directly related to the concentration of CHPMZ.

$$R = k[\text{CHPMZ}]^n \text{ and } \log I = n\log[\text{CHPMZ}] + \log k \quad (3)$$

3.7. Scan rate study

To understand the kinetics of the CHPMZ oxidation reaction at the BYSO/SPCE, CV was run at different scan rates. Fig. 7A shows the CV curves recorded at BYSO/SPCE for 150 μM CHPMZ in 0.05 M PBS (pH 7.0) at different potential scan rates from 20 to 200 mV/s. The peak current associated with the oxidation of CHPMZ increases steadily with increasing scan rate from 20 to 200 mV/s. Moreover, a good linear relationship was observed when the anodic peak current was plotted as a function of scan rate. The corresponding linear plot is shown in Fig. 7B along with the linear regression equation I_{pa} (μA) = 0.099 ν (mV/s) + 3.189 (R^2 = 0.992). This result shows that the electrochemical oxidation of CHPMZ on BYSO/SPCE is an adsorption-controlled process. Moreover, the peak potential of CHPMZ shifted to more positive values with an increasing scan rate. A linear relationship was obtained when the peak potential was plotted against the logarithm of the scan rate, as shown in Fig. S3B. The slope of this curve can be related to the relationship given in Equation (4) [44], where R, T, and F are the gas constant, thermodynamic temperature, and Faraday constant, respectively, α is the electron transfer coefficient, and n is the number of electrons transferred. Using the slope of 0.058 V (Fig. S3B), αn was estimated to be 1.010. Replacing α by 0.5 (for an irreversible electrochemical reaction), the number of electrons transferred during the electrochemical oxidation of CHPMZ was determined to be 2.0.

$$E_{pa}/\log \nu = 2.3\ RT/(1-\alpha)nF \quad (4)$$

In addition, the heterogeneous rate constant K^0 can be calculated using the following equation from Bard and [45] Faulkner (5).

$$I_p = 0.227\ n\ F\ A\ C^*\ K^0 \exp\left[-\alpha nF/RT\ (E_p - E^0)\right] \quad (5)$$

In this analysis, n, F, A, and C* have their usual meanings: Number of electrons (n = 2), Faraday constant (F = 96485.3), surface area (0.08 cm^2), and concentration of CHPMZ (C* = 150 μM/L). E^0 is the formal potential obtained by extrapolating the linear plot (Fig. S3B) of the log scan rate versus E_{pa} to ν = 0.

Fig. S3C shows the linear plot between ln I_{pa} and $E_{pa}-E^0$ along with the linear regression equation: ln I_{pa} (μA) = 25.704 ($E_{pa}-E^0$) +1.417 (R^2 = 0.996). From the linear regression equation, K^0 is related to the observed intercept of this equation. Based on equation (5), the heterogeneous rate constant (K^0) was calculated to be 4.49 × 10^{-3} cm/s and proves that the electrochemical oxidation of CHPMZ on BYSO/SPCE is a quasi-reversible reaction.

$$I_{pa} = n^2F^2rA\nu/4RT \quad (6)$$

In addition, the surface concentration of CPHMZ adsorbed on the BYSO/SPCE was calculated using Equation (6), where r represents the surface concentration of CPHMZ on the SPCE modified with BYSO. Using the slope of the I_{pa} vs. ν plot, Fig. 7B, r was calculated as 4.88 × 10^{-10} mol/cm^2.

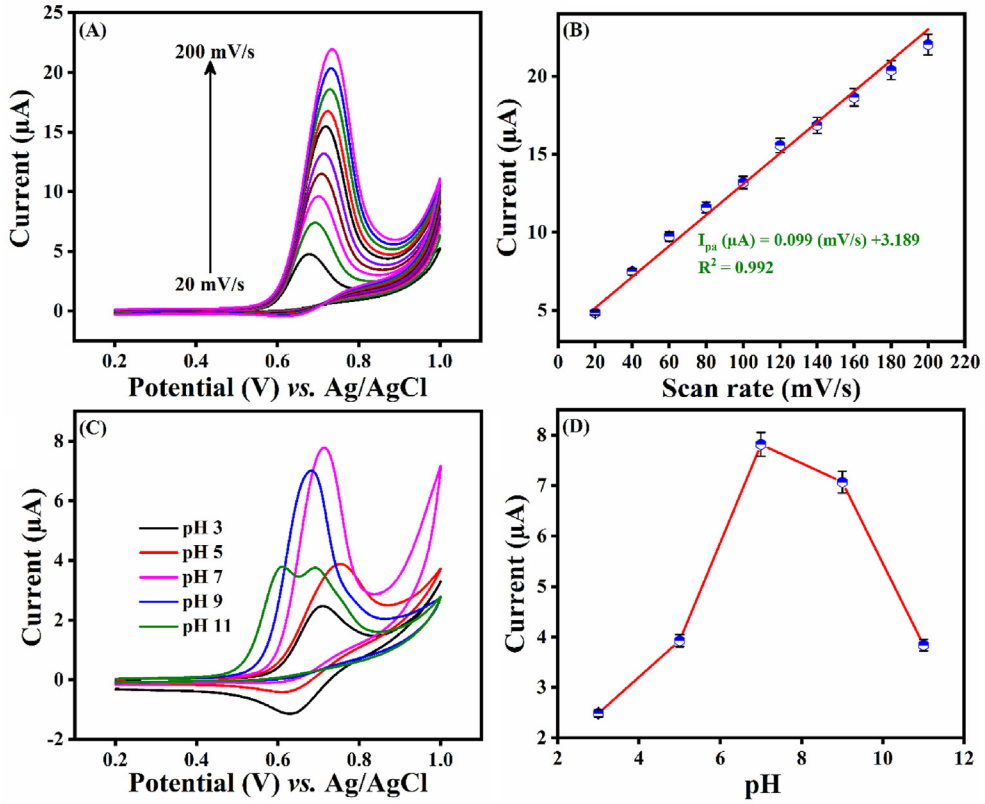

Fig. 7. (A) CVs of 150 μM CHPMZ on BYSO/SPCE at different scan rates (20–200 mV/s) in 0.05 M PBS (pH 7.0). (B) Calibration plot between the peak current of CHPMZ and the different scan rates. (C) CV curves of 150 μM CHPMZ in 0.05 PBS with different pH values (pH – 3.0, 5.0, 7.0, 9.0 and 11.0) on BYSO/SPCE (CV parameters: scan rate – 50 mV/s, potential – +0.2 V to +1.0 V). (D) Comparison of histograms of CHPMZ peak currents with respect to the different pH values.

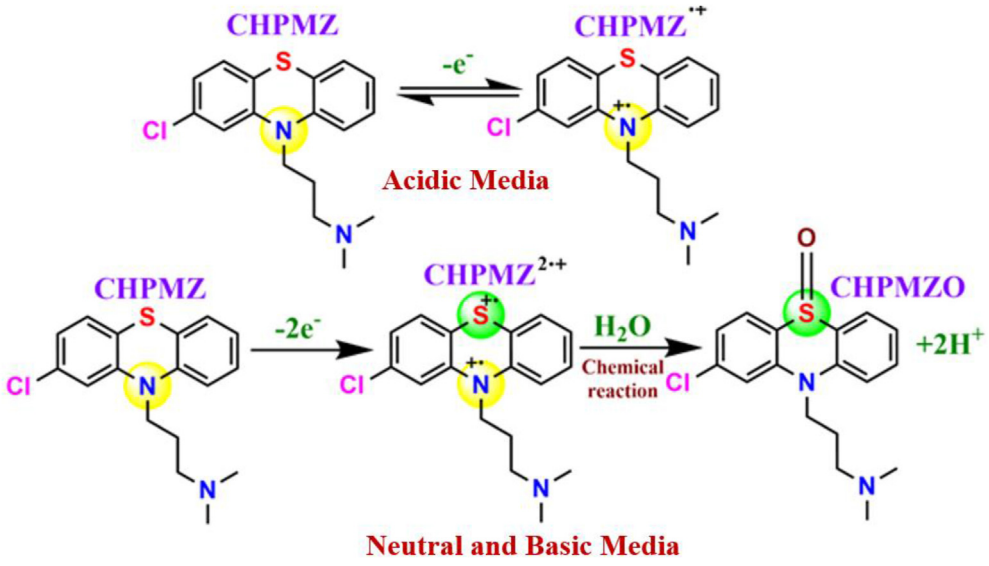

Scheme 2. Schematic representation of the electrochemical oxidation mechanism of CHPMZ at BYSO/SPCE.

3.8. Optimization of pH

In an electrochemical reaction, the peak current, peak potential, and peak shape can be affected by the pH of the electrolyte. Therefore, optimization of the pH of the electrolyte is an essential parameter in the development of electrochemical sensors. To find and optimize the most suitable pH for the CHPMZ sensor, the pH of the PBS was varied. Fig. 7C shows the CV curves recorded in 150 μM CHPMZ in 0.05 M PBS with different pH values from 3.0 to 11.0 at a scan rate of 50 mV/s. The pH of the solution significantly affects the oxidation of CHPMZ. At pH 11.0, a broad peak with two overlapping waves is seen. A reduction wave occurs in the more acidic solution, indicating some reversibility. Nevertheless, a well-resolved anodic peak is observed at all pH values, with pH affecting the peak current. Fig. 7D shows the anodic peak current plotted as a function of pH. The highest peak current was observed in a solution with a pH of 7.0. Therefore, a neutral electrolyte was chosen for all electrochemical sensing studies with CHPMZ.

3.9. Electrochemical oxidation mechanism of CHPMZ on BYSO/SPCE

From the scan rate study, the number of electrons transferred during electrochemical oxidation of CHPMZ at pH 7.0 is two. This result is consistent with Scheme 2, in which the nitrogen atom in CHPMZ is oxidized to the cation radical ($CHPMZ^{+\bullet}$), followed by the oxidation of the sulfur atom to form the dication radical ($CHPMZ^{2+\bullet}$) [46]. Moreover, the electrically generated dication undergoes a chemical reaction, which explains the irreversible nature of the oxidation of CHPMZ at neutral pH and pH values of 9.0 and 11.0 (Fig. 7C). This irreversible oxidation reaction occurs in neutral and basic media by directly transferring two electrons [47]. However, at pH 11.0, two overlapping peaks are observed, which can be explained by the relative oxidation potentials of the N and S atoms in this more alkaline solution. At neutral pH, the formation of $CHPMZ^{+\bullet}$ and $CHPMZ^{2+\bullet}$ occurs at similar potentials, whereas at pH 11.0, the oxidation potentials diverge somewhat, with the formation of $CHPMZ^{+\bullet}$ appearing at about 0.59 V (Fig. 7C). In contrast, reversibility is observed at pH 3.0 due to the reduction of the cation radical $CHPMZ^{+\bullet}$ to CHPMZ. In this acidic medium, the electrochemical oxidation of CHPMZ to BYSO/SPCE is a reversible reaction with electron transfer ($CHPMZ^{+\bullet}$). Since the $CHPMZ^{+\bullet}$ is less stable with increasing pH, this reversibility is lost at higher pH values (Fig. 7C).

3.10. Analytical performance of BYSO/SPCE for CHPMZ

The analytical performance of BYSO/SPCE for the electrochemical detection of CHPMZ was investigated using DPV. The selected potential window for the DPV experiment was between +0.2 and +1.0 V. Representative DPV curves for different

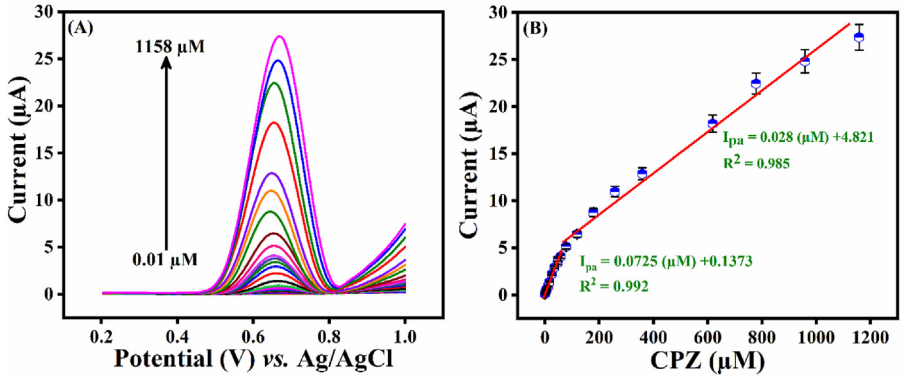

Fig. 8. (A) DPV curves BYSO/SPCE for the different concentrations of CHPMZ in 0.05 M PBS (pH 7.0). (B) Calibration plot between DPV current (I_{pa}) and concentration of CHPMZ.

Table 1
Determination of CHPMZ based on different electrodes.

Electrode	Technique	Linear range (μM)	LOD (nM)	Sensitivity (μA/μM/cm^2)	Ref.
GPE[a]	DPV	0.01–9.00	6	Not given	[48]
MWCNT-PEI[b]	DPV	0.019–9.2	10	1.3	[49]
CdO/NPs/IL/CPE[c]	SWV	1–350	70	Not given	[50]
PGE[d]	DPV	0.01–0.08	3	Not given	[46]
TVGCPE[e]	DPV	0.03–850	5.9	Not given	[51]
Cys/CPE[f]	DPV	1–35	10	Not given	[52]
GO-Fe/ZnO[h]	DPV	0.02–1047.7	20	7.56	[53]
N-CDs[g]/Cu_2O	DPV	0.001–230	25	Not given	[47]
WS_2	DPV	0–690	4	1.416 μA/mM/cm^2	[54]
BYSO/SPCE	DPV	0.01–58.41, 78.41–1158	3	1.03	This work

[a] Graphene paste electrode.
[b] Multiwall carbon nanotube-polyethyleneimine.
[c] Cadmium oxide NPs/ionic liquid/carbon paste electrode.
[d] Pencil graphite electrode.
[e] TiO_2/V_2O_5/Graphene/carbon paste electrode.
[f] L-Cystine/Carbon paste electrode.
[g] Nitrogen-doped carbon dots.
[h] Aerogel composite material.

concentrations of CHPMZ are shown in Fig. 8A. A significant increase in peak current can be seen as the CHPMZ concentration increases from 0.01 to 1158 μM. Two linear regions were observed when recording the peak current as a function of CHPMZ concentration, as shown by the calibration curve in Fig. 8B, which shows the two linear response ranges. At lower concentrations, the linear range extends from 0.01 to 58.41 μM, which has the correlation regression equation I_{pa} (μA) = 0.072C (μM) +0.137 (R^2 = 0.992). At higher concentrations, the linear range of 78.41–1158 μM was determined, for which the calibration equation is I_{pa} = 0.028C (μM) + 4.8217 (R^2 = 0.985). The two linear ranges may be related to the formation of oxidation products of CHPMZ, which can form and accumulate on the surface of the electrode. The extent of accumulation depends on the CHPMZ concentration, which affects the further oxidation of CHPMZ at the BYSO/SPCE. Based on the linear range at the lower concentrations, the detection limit (LOD) and sensitivity of the BYSO/SPCE for CHPMZ detection were determined. According to Equation (6), the LOD of CHPMZ on BYSO/SPCE was estimated to be 0.003 μM.

$$LOD = 3S/B \quad (7)$$

In equation (7), S – represents the standard deviation (determined from 3 DPV blank value curves), and B represents the correlation slope determined from the lower linear range. In addition, the sensitivity of the BYSO/SPCE sensor was calculated to be 1.03 μA/μM/cm^2. The resulting analytical parameters such as the linear ranges, sensitivity, and LOD of the assembled BYSO/SPCE sensor for CHPMZ were compared with the previously reported CHPMZ sensor using different electrodes and analytical techniques and are listed in Table 1 [46–54]. This comparative analysis shows that the developed BYSO/SPCE sensor has a wide linear range, higher sensitivity, and lower detection limits than the previously fabricated sensors, indicating that the BYSO modified SPCE is an efficient sensor for the determination of CHPMZ.

3.11. Influence of coexisting substances, repeatability, and stability studies of CHPMZ sensors

The selectivity of the BYSO/SPCE sensor was evaluated by the DPV method under optimal conditions with biologically active

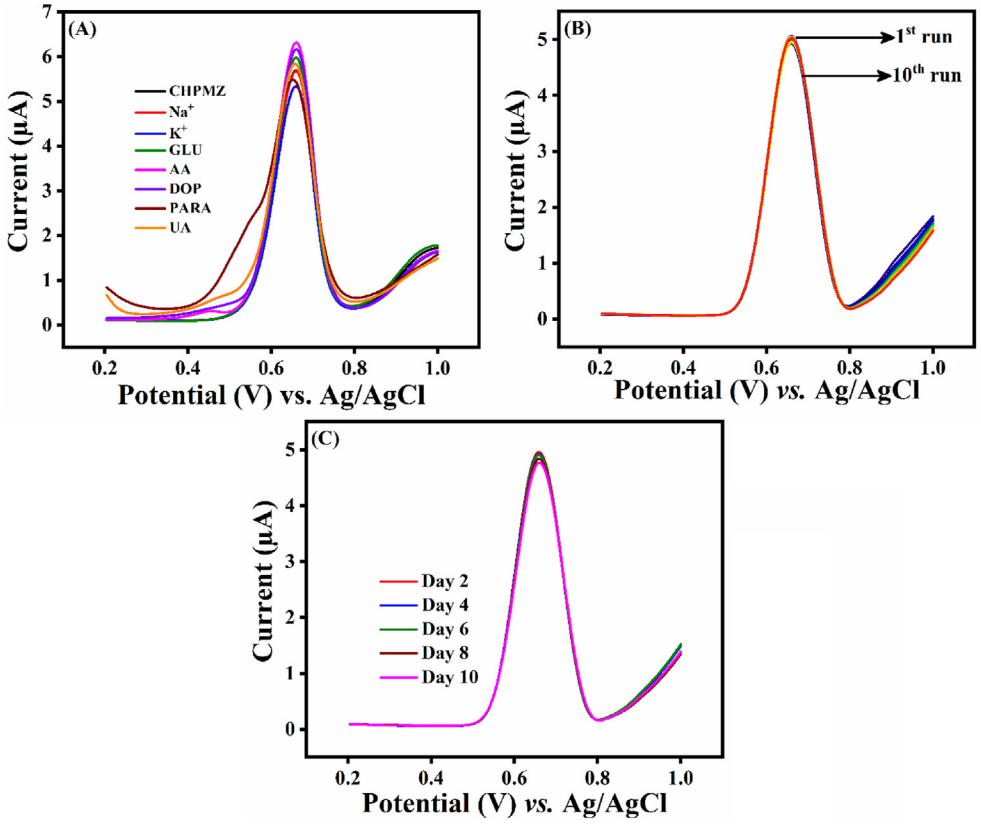

Fig. 9. (A) Interference study of BYSO/SPCE in 0.05 M PBS (pH 7.0) containing 100 μM CHPMZ together with Na^+, K^+, GLU, AA, DOP, UA, PARA. (B) Repeatability of 100 μM CHPMZ in 0.05 M PBS (pH 7.0) in BYSO/SPCE. (C) Stability study of BYSO/SPCE against 100 μM CHPMZ.

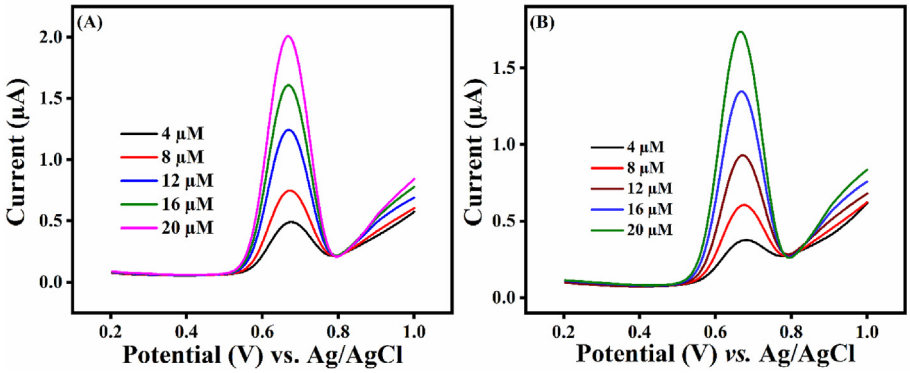

Fig. 10. (A) Real sample study of CHPMZ based on BYSO/SPCE (A) Blood serum, (B) Urine sample.

molecules such as glucose (GLU), ascorbic acid (AA), uric acid (UA), dopamine (DOP), Na^+, K^+, and acetaminophen (PARA) as interfering species. Fig. 9A shows the DPV current response of 100 μM CHPMZ and a 3-fold excess (300 μM) of the above interfering species in 0.05 M PBS. The oxidation of PARA is seen at +0.45 V and overlaps with the oxidation of CHPMZ. However, no significant differences were observed in the peak current and peak potential of CHPMZ. When interference was present, the anodic peak current response for CHPMZ showed a maximum deviation of less than 5% compared to CHPMZ. This result indicates that the BYSO/SPCE sensor has reasonable selectivity for CHPMZ in the presence of multiple biologically active components. The repeatability of the constructed CHPMZ sensor was analyzed by recording ten consecutive DPV experiments with a single BYSO/SPCE. These repeatability experiments are summarized in Fig. 9B, which shows the DPV response of 100 μM CHPMZ in 0.05 M PBS at pH 7.0. It was observed that the anodic current response decreased by only 2% after the 10th cycle of the DPV experiment, indicating excellent repeatability. Furthermore, the stability of the developed BYSO/SPCE sensors was analyzed using DPV after different storage times. As shown in Fig. 9C, the peak currents recorded in 100 μM CHPMZ in 0.05 M PBS (pH 7.0) varied very little from day 2 to day 10, with only a 2% decrease in current response after the 10-day storage period. From these studies, it can be concluded that the BYSO/SPCE sensors have sufficient selectivity in the presence of active biological components and exhibit excellent repeatability and storage stability over ten days.

3.12. Determination of CHPMZ in biological fluids

The developed BYSO/SPCE sensor has a wide dynamic linear range, low detection limit, high sensitivity, excellent repeatability, good storage stability, and reasonable selectivity. Therefore, the sensor was used to test its performance in the determination of CHPMZ in more complex biological fluids. DPV experiments were performed in blood serum and urine samples to evaluate these practical applications. Following the procedure described in Section 2.4, the stock solution of the real samples was prepared and used for the DPV experiments. Fig. 10A and B shows the DPV curves for the analysis of CHPMZ in the blood and urine samples. In this case, different concentrations of CHPMZ were added to the biological fluids. The anodic current increases with increasing concentration from 4 to 20 μM CHPMZ. The spiking and recovery rates of the constructed CHPMZ sensor in the biological samples are summarized in Table S1. They show 86–107% recoveries and 85–103% in the blood serum and urine samples, respectively. These results indicate that the constructed BYSO/SPCE sensor is efficient and suitable for the determination of CHPMZ in real samples.

4. Conclusion

The defective BYSO NPs were prepared by a simple co-precipitation technique followed by thermal treatment. The electrocatalytic activity of the BYSO NPs was analyzed to detect and determine CHPMZ, an antipsychotic drug. The presence of various ionic centers and the defect nature of BYSO NPs improve the electrochemical performance of BYSO, resulting in a low detection limit of 3 nM and a high sensitivity of 1.03 μA/μM/cm^2 in the detection of CHPMZ. The sensor thus developed shows good selectivity, repeatability, and stability in the determination of CHPMZ. Moreover, good recovery results were obtained in the analysis of CHPMZ in human blood serum and urine samples.

CRediT authorship contribution statement

Raj Karthik: Conceptualization, Methodology, Experimental operation, Data curation, Analysis, Writing - original draft. **Karuppiah Balamurugan**: Conceptualization, Methodology, Investigation, Validation, Data curation, Analysis, Writing-original draft. **Shen-Ming Chen**: Supervision, Investigation, Funding acquisition, Writing - review & editing. **Ramaraj Sukanya**: Writing - original draft, review & editing, Software, Formal analysis, **Prajakta R. Chavan**: Formal analysis, Data analysis, Writing - review & editing. **Van Quang Nguyen**: Formal analysis, Methodology, Data curation, Software, **Jae-Jin Shim**: Supervision, Project administration, Investigation, Funding acquisition. **Carmel B. Breslin**: Supervision, Investigation, Writing - review & editing.

Declaration of competing interest

The authors declare that they have no known competing financial interests or personal relationships that could have appeared to influence the work reported in this paper.

Data availability

Data will be made available on request.

Acknowledgments

The authors acknowledge the Ministry of Science and Technology (MOST 110-2113-M-027-003). This study was supported by Science Foundation Ireland under grant number SFI/20/FFP-P/8793 and the National Research Foundation (NRF) of the Republic of Korea under the frameworks of the Priority Research Centers Program (NRF-2014R1A6A1031189) and the Regional University

Superior Scientist Research Program (NRF-2020R1I1A3073981) funded by the Ministry of Education, the Republic of Korea.

Appendix A. Supplementary data

Supplementary data to this article can be found online at https://doi.org/10.1016/j.mtchem.2022.101117.

References

[1] D. Daniel, I.G.R. Gutz, Spectroelectrochemical determination of chlorpromazine hydrochloride by flow-injection analysis, J. Pharm. Biomed. 37 (2005) 281–286, https://doi.org/10.1016/j.jpba.2004.10.048.

[2] E.Y. Frag, M.A. Zayed, M.M. Omar, S.E. Elashery, G.G. Mohamed, Potentiometric determination of chlorpromazine HCl using carbon paste electrode in pure and pharmaceutical preparations, Int. J. Electrochem. Sci. 7 (2012) 650–662.

[3] J.V. Kumar, R. Karthik, S.M. Chen, T. Kokulnathan, S. Sakthinathan, V. Muthuraj, T.W. Chiu, T.W. Chen, Highly selective electrochemical detection of antipsychotic drug chlorpromazine in drug and human urine samples based on peas-like strontium molybdate as an electrocatalyst, Inorg. Chem. Front. 5 (2018) 643–655, https://doi.org/10.1039/c7qi00743d.

[4] A.A. Ensafi, E. Heydari, Determination of some phenothiazines compounds in pharmaceuticals and human body fluid by electrocatalytic oxidation at a glassy carbon electrode using methylene blue as a mediator, Anal. Lett. 41 (13) (2008) 2487–2502, https://doi.org/10.1080/00032710802352555.

[5] S.M. Sultan, Computer-assisted optimization of a flow-injection method for the assay of promethazine, chlorpromazine and trimeprazine in drug formulations, Talanta 40 (1993) 681–686, https://doi.org/10.1016/0039-9140(93)80278-Y.

[6] D. Stevenson, E. Reid, Determination of chlorpromazine and its sulfoxide and 7-hydroxy metabolites by ion-pair high-pressure liquid chromatography, Anal. Lett. 14 (1981) 741–761, https://doi.org/10.1080/00032718108055479.

[7] H. Reza Sobhi, Y. Yamini, R.H.H. Baghdad Abadi, Extraction and determination of trace amounts of chlorpromazine in biological fluids using hollow fiber liquid phase microextraction followed by high-performance liquid chromatography, J. Pharm. Biomed. 45 (2007) 769–774, https://doi.org/10.1016/j.jpba.2007.09.026.

[8] M.G. Sales, J.F. Tomas, S.R. Lavandeira, Flow injection potentiometric determination of chlorpromazine, J. Pharm. Biomed. 41 (2006) 1280–1286, https://doi.org/10.1016/j.jpba.2006.03.027.

[9] G. Xu, S. Dong, Electrochemiluminescent detection of chlorpromazine by selective preconcentration at a lauric acid-modified carbon paste electrode using tris(2,2'-bipyridine)ruthenium(II), Anal. Chem. 72 (2000) 5308–5312, https://doi.org/10.1021/ac000507s.

[10] F.J. Lara, A.M. García-campaña, F. Alés-barrero, J.M. Bosque-sendra, Development and validation of a capillary electrophoresis method for the determination of phenothiazines in human urine in the low nanogram per milliliter concentration range using field- amplified sample injection, Electrophoresis 26 (12) (2005) 2418–2429, https://doi.org/10.1002/elps.200500098.

[11] E. Aleshin, R. Roy, Crystal chemistry of pyrochlore, J. Am. Ceram. Soc. 45 (1) (1962) 18–25, https://doi.org/10.1111/j.1151-2916.1962.tb11022.x.

[12] E.J. Harvey, K.R. Whittle, G.R. Lumpkin, R.I. Smith, S.A.T. Redfern, Solid solubilities of $(La\ Nd,)_2(Zr,\ Ti)_2O_7$ phases deduced by neutron diffraction, J. Solid State Chem. 178 (2005) 800–810, https://doi.org/10.1016/j.jssc.2004.12.030.

[13] J.B. Goodenough, R.N. Castellano, Defect pyrochlores as catalyst supports, J. Solid State Chem. 44 (1982) 108–112, https://doi.org/10.1016/0022-4596(82)90406-6.

[14] F. Matteucci, G. Cruciani, M. Dondi, G. Baldi, A. Barzanti, Crystal structural and optical properties of Cr-doped $Y_2Ti_2O_7$ and $Y_2Sn_2O_7$ pyrochlores, Acta Mater. 55 (2007) 2229–2238, https://doi.org/10.1016/j.actamat.2006.11.008.

[15] Q. Wu, Y. Liu, H.G. Wang, J. Hou, Y. Li, Q. Duan, Graphene encapsulated metallic state $Ce_2Sn_2O_7$ as a novel anode material for superior lithium-ion batteries and capacitors, J. Mater. Chem. A. 8 (2020) 5517–5524, https://doi.org/10.1039/c9ta13086a.

[16] B. Muthukutty, J. Ganesamurthi, T.W. Chen, S.M. Chen, J. Yu, X. Liu, A novel high-performance electrocatalytic determination platform for voltammetric sensing of eugenol in acidic media using pyrochlore structured lanthanum stannate nanoparticles, J. Ind. Eng. Chem. 106 (2022) 103–112, https://doi.org/10.1016/j.jiec.2021.10.015.

[17] R. Rajakumaran, R. Sukanya, S.M. Chen, R. Karthik, C.B. Breslin, P.M. Shafi, Synthesis and characterization of pyrochlore-type praseodymium stannate nanoparticles: an effective electrocatalyst for detection of nitrofurazone drug in biological samples, Inorg. Chem. 60 (2021) 2464–2476, https://doi.org/10.1021/acs.inorgchem.0c03377.

[18] R. Rajakumaran, K. Balamurugan, S.M. Chen, R. Sukanya, Facile synthesis of neodymium stannate nanoparticles an effective electrocatalyst for the selective detection of dimetridazole in biological samples, Anal. Chim. Acta 1190 (2022), 339234, https://doi.org/10.1016/j.aca.2021.339234.

[19] K. Balamurugan, R. Rajakumaran, S.M. Chen, T.W. Chen, P.J. Huang, Co-precipitation synthesis and characterization of rare-earth pyrochlore Gadolinium stannate; A novel electrocatalyst for the determination of furazolidone in water samples, Int. J. Electrochem. Sci. 16 (2021) 1–20, https://doi.org/10.20964/2021.03.20.

[20] R. Rajakumaran, K. Balamurugan, S.M. Chen, R. Sukanya, C.B. Breslin, Electrocatalytic studies of coral-shaped samarium stannate nanoparticles for selective detection of azathioprine in biological samples, ACS Appl. Nano Mater. 4 (2021) 13048–13059, https://doi.org/10.1021/acsanm.1c02591.

[21] J.T. Mefford, X. Rong, A.M. Abakumov, W.G. Hardin, S. Dai, A.M. Kolpak, K.P. Johnston, K.J. Stevenson, Water electrolysis on $La_{1-x}Sr_xCoO_{3-\delta}$ perovskite electrocatalysts, Nat. Commun. 7 (2016), https://doi.org/10.1038/ncomms11053.

[22] K. Li, H. Wang, H. Yan, Hydrothermal preparation and photocatalytic properties of $Y_2Sn_2O_7$ nanocrystals, J. Mol. Catal. Chem. 249 (2006) 65–70, https://doi.org/10.1016/j.molcata.2006.01.002.

[23] H. Peng, J. Xu, J. Tian, Y. Liu, Y. He, J. Tan, X. Xu, W. Liu, N. Zhang, X. Wang, Mesoporous $Y_2Sn_2O_7$ pyrochlore with exposed (111) facets: an active and stable catalyst for CO oxidation, RSC Adv. 6 (75) (2016) 71791–71799, https://doi.org/10.1039/c6ra11826g.

[24] P. Nithyadharseni, M.V. Reddy, K.I. Ozoemena, R.G. Balakrishna, B.V.R. Chowdari, Low temperature molten salt synthesis of $Y_2Sn_2O_7$ anode material for lithium ion batteries, Electrochim. Acta 182 (2015) 1060–1069, https://doi.org/10.1016/j.electacta.2015.10.004.

[25] N. Sharma, G.V.S. Rao, B.V.R. Chowdari, Anodic properties of tin oxides with pyrochlore structure for lithium-ion batteries, J. Power Sources 159 (2006) 340–344, https://doi.org/10.1016/j.jpowsour.2006.04.050.

[26] M. Kim, J. Park, M. Kang, J.Y. Kim, S.W. Lee, Toward efficient electrocatalytic oxygen evolution: emerging opportunities with metallic pyrochlore oxides for electrocatalysts and conductive supports, ACS Cent. Sci. 6 (6) (2020) 880–891, https://doi.org/10.1021/acscentsci.0c00479.

[27] A.A. Ansari, M.K. Nazeeruddin, M.M. Tavakoli, Organic-inorganic upconversion nanoparticles hybrid in dye-sensitized solar cells, Coord. Chem. Rev. 436 (2021), 213805, https://doi.org/10.1016/j.ccr.2021.213805.

[28] A.A. Ansari, S.F. Adil, M. Alam, N. Ahmad, M.E. Assal, J.P. Labis, A. Alwarthan, Catalytic performance of the Ce-doped $LaCoO_3$ perovskite nanoparticles, Sci. Rep. 10 (2020) 1–13, https://doi.org/10.1038/s41598-020-71869-z.

[29] A.A. Ansari, N. Ahmad, M. Alam, S.F. Adil, S.M. Ramay, A. Albadri, A. Ahmad, A.M. Al-Enizi, B.F. Alrayes, M.E. Assal, A.A. Alwarthan, Physico-chemical properties and catalytic activity of the sol-gel prepared Ce-ion doped $LaMnO_3$ perovskites, Sci. Rep. 9 (2019) 1–12, https://doi.org/10.1038/s41598-019-44118-1.

[30] J. Kim, P. Shih, Y. Qin, Z. Al-Bardan, C. Sun, H. Yang, A porous pyrochlore $Y_2[Ru_{1.6}Y_{0.4}]O_{7-\delta}$ electrocatalyst for enhanced performance towards the oxygen evolution reaction in acidic media, Angew. Chem. 130 (2018) 14073–14077, https://doi.org/10.1002/ange.201808825.

[31] D.A. Kuznetsov, M.A. Naeem, P.V. Kumar, P.M. Abdala, A. Fedorov, C.R. Müller, Tailoring lattice oxygen binding in ruthenium pyrochlores to enhance oxygen evolution activity, J. Am. Chem. Soc. 142 (2020) 7883–7888, https://doi.org/10.1021/jacs.0c01135.

[32] D.A. Kuznetsov, J. Peng, L. Giordano, Y. Román-Leshkov, Y. Shao-Horn, Bismuth substituted strontium cobalt perovskites for catalyzing oxygen evolution, J. Phys. Chem. C 124 (2020) 6562–6570, https://doi.org/10.1021/acs.jpcc.0c01401.

[33] A. Alemi, R.E. Kalan, Preparation and characterization of neodymium tin oxide pyrochlore nanocrystals by the hydrothermal method, Radiat. Eff. Defect Solid 163 (3) (2008) 229–236, https://doi.org/10.1080/10420150801976436.

[34] K. Balamurugan, R. Rajakumaran, S.M. Chen, R. Karthik, J.J. Shim, P.M. Shafi, Massive engineering of spinel cobalt tin oxide/tin oxide-based electrocatalyst for the selective voltammetric determination of antibiotic drug furaltadone in water samples, J. Alloys Compd. 882 (2021), 160750, https://doi.org/10.1016/j.jallcom.2021.160750.

[35] D. Li, J. Xue, Synthesis of $Bi_2Sn_2O_7$ and enhanced photocatalytic activity of $Bi_2Sn_2O_7$ hybridized with C_3N_4, New J. Chem. 39 (2015) 5833–5840, https://doi.org/10.1039/c5nj00886g.

[36] W. Xu, G. Zhou, J. Fang, Z. Liu, Y. Chen, C. Cen, Synthesis and characterization of pyrochlore $Bi_2Sn_2O_7$ doping with praseodymium by hydrothermal method and its photocatalytic activity study, Int. J. Photoenergy 2013 (2013), https://doi.org/10.1155/2013/234806.

[37] L. Sun, J. Pan, X. Zhang, H. Wang, L. Li, Y. Yu, Synthesis, morphology and spectroscopic properties of red-luminescent rhombohedral YOF: Yb^{3+}, Er^{3+} powders, RSC Adv. 5 (95) (2015) 77673–77681, https://doi.org/10.1039/c5ra12357g.

[38] W. Cun, W. Xinming, Synthesis, characterization and photocatalytic property of nano-sized Zn_2SnO_4, J. Mater. Sci. 37 (14) (2002) 2989–2996, https://doi.org/10.1023/A:1016077216172.

[39] M. Asif, M. Zafar, P. Akhter, M. Hussain, W.Y. Kim, A. Umer, A. Razzaq, Effect of urea addition on anatase phase enrichment and nitrogen doping of TiO_2 for photocatalytic abatement of methylene blue, Appl. Sci. 11 (2021) 1–15, https://doi.org/10.3390/app11178264.

[40] P. Jia, X. Yu, J. Lu, X. Zhou, Z. Yin, G. Tang, T. Lu, L. Guo, L. Song, B. Wang, Y. Hu, The $Re_2Sn_2O_7$ (Re = Nd, Sm, Gd) on the enhancement of fire safety and physical performance of Polyolefin/IFR cable materials, J. Colloid Interface Sci. 608 (2022) 1652–1661, https://doi.org/10.1016/j.jcis.2021.10.114.

[41] T. Hu, D. Ma, Q. Fang, P. Zhang, X. Liu, R. Wei, Y. Pan, K. Xu, F. Ma, Bismuth mediated defect engineering of epitaxial graphene on SiC(0001), Carbon 146 (2019) 313–319, https://doi.org/10.1016/j.carbon.2019.02.014.

[42] R. Trujillano, J.A. Martín, V. Rives, Hydrothermal synthesis of $Sm_2Sn_2O_7$ pyrochlore accelerated by microwave irradiation. A comparison with the solid state synthesis method, Ceram. Int. 42 (2016) 15950–15954, https://doi.org/10.1016/j.ceramint.2016.07.090.

[43] P.J. Wilde, C.R.A. Catlow, Defects and diffusion in pyrochlore structured oxides, Solid State Ionics 112 (1998) 173–183, https://doi.org/10.1016/s0167-2738(98)00190-8.
[44] E. Laviron, General expression of the linear potential sweep voltammogram in the case of diffusionless electrochemical systems, J. Electroanal. Chem. 101 (1979) 19–28, https://doi.org/10.1016/S0022-0728(79)80075-3.
[45] S.A. Maier, Plasmonics: Fundamentals and Applications, Springer, New York, 2007. http://elib.tu-darmstadt.de/tocs/95069577.pdf.
[46] H.T. Purushothama, Y.A. Nayaka, M.M. Vinay, P. Manjunatha, R.O. Yathisha, K.V. Basavarajappa, Pencil graphite electrode as an electrochemical sensor for the voltammetric determination of chlorpromazine, J. Sci. Adv. Mater. Devices 3 (2018) 161–166, https://doi.org/10.1016/j.jsamd.2018.03.007.
[47] V.N. Palakollu, R. Karpoormath, L. Wang, J.N. Tang, C. Liu, A versatile and ultrasensitive electrochemical sensing platform for detection of chlorpromazine based on nitrogen-doped carbon dots/cuprous oxide composite, Nanomaterials 10 (2020) 1–15, https://doi.org/10.3390/nano10081513.
[48] M.H. Parvin, Graphene paste electrode for detection of chlorpromazine, Electrochem. Commun. 13 (2011) 366–369, https://doi.org/10.1016/j.elecom.2011.01.027.
[49] B. Unnikrishnan, P.C. Hsu, S.M. Chen, A multipurpose voltammetric sensor for the determination of chlorpromazine in presence of acetaminophen, uric acid, dopamine and ascorbic acid, Int. J. Electrochem. Sci. 7 (2012) 11414–11425.
[50] S. Ahmadzadeh, F. Karimi, N. Atar, E.R. Sartori, E. Faghih-Mirzaei, E. Afsharmanesh, Synthesis of CdO nanoparticles using direct chemical precipitation method: fabrication of novel voltammetric sensor for square wave voltammetry determination of chlorpromazine in pharmaceutical samples, Inorg. Nano-Metal Chem. 47 (2017) 347–353, https://doi.org/10.1080/15533174.2016.1186049.
[51] N. Tavakkoli, N. Soltani, H. Salavati, M. Talakoub, New carbon paste electrode modified with graphene/TiO_2/V_2O_5 for electrochemical measurement of chlorpromazine hydrochloride, J. Taiwan Inst. Chem. Eng. 83 (2018) 50–58, https://doi.org/10.1016/j.jtice.2017.12.012.
[52] H.T. Purushothama, Y. Arthoba Nayaka, P. Manjunatha, R.O. Yathisha, M.M. Vinay, K.V. Basavarajappa, Electrochemical determination of chlorpromazine using L-Cysteine modified carbon paste electrode, Chem. Data Collect. 23 (2019), 100268, https://doi.org/10.1016/j.cdc.2019.100268.
[53] N. Sebastian, W.C. Yu, Y.C. Hu, D. Balram, Y.H. Yu, Sonochemical synthesis of iron-graphene oxide/honeycomb-like ZnO ternary nanohybrids for sensitive electrochemical detection of antipsychotic drug chlorpromazine, Ultrason. Sonochem. 59 (2019), 104696, https://doi.org/10.1016/j.ultsonch.2019.104696.
[54] N. Subramanian, K.M. Priya, M.O. Valappil, N. Nesakumar, S. Kesavan, S. Alwarappan, Electrochemically exfoliated porous WS_2 nanosheets: a potential electrochemical sensing platform for chlorpromazine detection, J. Electrochem. Soc. 166 (2019) B749–B755, https://doi.org/10.1149/2.1301908jes.
[55] J. Tang, Z.Z. Hui, T. Hu, X. Cheng, J.H. Guo, Z.R. Li, H. Yu, A sensitive acetaminophen sensor based on Co metal-organic framework (ZIF-67) and macroporous carbon composite, Rare Met. 41 (2022) 189–198, https://doi.org/10.1007/s12598-021-01709-0.